Monthly Notices
of the
ROYAL ASTRONOMICAL SOCIETY

MNRAS **459,** 2790–2805 (2016)
Advance Access publication 2016 March 23

doi:10.1093/mnras/stw691

The minimum mass of detectable planets in protoplanetary discs and the derivation of planetary masses from high-resolution observations

Giovanni P. Rosotti,* Attila Juhasz, Richard A. Booth and Cathie J. Clarke
Institute of Astronomy, University of Cambridge, Madingley Road, Cambridge CB3 0HA, UK

Accepted 2016 March 21. Received 2016 March 21; in original form 2016 January 22

ABSTRACT

We investigate the minimum planet mass that produces observable signatures in infrared scattered light and submillimetre (submm) continuum images and demonstrate how these images can be used to *measure* planet masses to within a factor of about 2. To this end, we perform multi-fluid gas and dust simulations of discs containing low-mass planets, generating simulated observations at 1.65, 10 and 850 μm. We show that the minimum planet mass that produces a detectable signature is $\sim$15 $M_\oplus$: this value is strongly dependent on disc temperature and changes slightly with wavelength (favouring the submm). We also confirm previous results that there is a minimum planet mass of $\sim$20 $M_\oplus$ that produces a pressure maximum in the disc: only planets above this threshold mass generate a dust trap that can eventually create a hole in the submm dust. Below this mass, planets produce annular enhancements in dust outwards of the planet and a reduction in the vicinity of the planet. These features are in steady state and can be understood in terms of variations in the dust radial velocity, imposed by the perturbed gas pressure radial profile, analogous to a traffic jam. We also show how planet masses can be derived from structure in scattered light and submm images. We emphasize that simulations with dust need to be run over thousands of planetary orbits so as to allow the gas profile to achieve a steady state and caution against the estimation of planet masses using gas-only simulations.

Key words: hydrodynamics – planet–disc interactions – protoplanetary discs – submillimetre: planetary systems.

1 INTRODUCTION

Planets form in the dense, rotationally flattened structures of dust and gas called 'protoplanetary disc' (see Williams & Cieza 2011 for a review). Despite the rapid expansion of our knowledge of exoplanets around main-sequence stars (Mayor & Queloz 1995), little is known about the putative planets that may already be present in such discs at an age of <10 Myr. The Atacama Large Millimeter/submillimeter Array (ALMA), which is approaching its full capability, can reach the unprecedented resolution and sensitivity necessary for the detailed characterization of such discs and may also be able to detect direct signatures of embedded protoplanets (see for example the pattern of bright and dark rings observed in HL Tau during a science verification campaign which has been interpreted as being of planetary origin; Brogan et al. 2015). The latest near-infrared (NIR) instruments on 8 m class telescopes [e.g. Spectro-Polarimetric High-contrast Exoplanet REsearch (SPHERE) on the Very Large Telescope (VLT) or Gemini Planet Imager (GPI) on the Gemini Telescope] provide an opportunity to search for planetary signatures in discs via scattered light imaging at similar resolution as ALMA in the submillimetre (submm). In the near future, similar resolution will be available in the thermal mid-infrared (MIR) when the 30–40 m class telescopes (e.g. the European Extremely Large Telescope, E-ELT) will come online.

It is very tempting to connect the presence of rings and gaps in protoplanetary disc images (which might be commonplace; see Zhang et al. 2016) to the presence of planets. According to conventional core accretion models (Pollack et al. 1996), however, giant planets are an unexpected outcome at the very young age ascribed to HL Tau (10^5 yr; Kenyon & Hartmann 1995). It is however currently unclear whether this indeed involves a revision of planet formation mechanisms and time-scales or whether the structures seen in the image are not planetary in origin. Our focus here however is not to add to the debate on this particular system but to present a more generic exploration of the detectability of planetary signatures via submm and scattered light imaging.

It is often assumed that only giant planets can create structures in discs prominent enough to be observed (e.g. Varnière et al. 2006; Ruge et al. 2013, 2014). Indeed, it is well known that giant planets create gaps in the *gas* disc (Lin & Papaloizou 1979), partially depleting the surface density in a region as wide as a few times its

*E-mail: rosotti@ast.cam.ac.uk

Hill radius. Planets with a mass smaller than a critical value, which is typically somewhat lower than the mass of Jupiter, are not able to open significant gaps (Crida, Morbidelli & Masset 2006), and one might then think that these objects would not produce observable features in discs. In this case, it would not be possible to put observational constraints on the formation conditions of the large population of super-Earths discovered by *Kepler* around main-sequence stars, objects now believed to constitute the most abundant population of planetary objects (Howard et al. 2012). This is particularly unfortunate because whereas it is clear that gas giant planets *must* form at an evolutionary stage when disc gas is still abundantly present, it is unclear whether super-Earths originate at similarly early times. Conventionally, terrestrial planet formation is often ascribed to later eras (age of ∼100 Myr) when the disc gas has long since dissipated and planet building proceeds via planetesimal collisions and giant impacts among embryos in a gas-poor environment (Raymond et al. 2014). On the other hand, the conventional core accretion scenario for gas giant planet formation (Pollack et al. 1996) envisages the formation of rock cores within the protoplanetary disc which only convert to gas giants if they attain a critical mass in excess of 10–20 Earth masses while gas is still abundantly present. An alternative model for super-Earth formation would therefore involve the assembly of rock cores during the disc phase, in the case that cores did not achieve criticality during the gas-rich phase. The core growth rate, and therefore the dichotomy that we observe for example in the Solar system between terrestrial and giant planets, might be due to the location in the disc with respect to the water snow line (Morbidelli et al. 2015). A conceptually distinct scenario for super-Earth formation instead invokes photoevaporation from the central star (on a time-scale of ∼100 Myr) to erode the gas envelope of a gas giant planet formerly produced in the protoplanetary disc (Owen & Wu 2013).

Here we explore whether planetary signatures can potentially be detected in the low-mass (super-Earth) regime. This issue has not received much attention to date since the impossibility of gap opening at masses much below a Jupiter mass (∼300 $M_\oplus$) implies that low-mass planets have only a modest effect on disc *gas* distributions. Nevertheless, a number of studies have indicated that planet-induced signatures are stronger in disc *dust* than in the gas, on account of the tendency of drag-coupled dust to collect in pressure maxima in the disc (Weidenschilling 1977). Such an effect has been shown to enhance the observability of structures produced by more massive planets, as dust becomes trapped at the outer edge of disc gaps (e.g. Rice et al. 2006; Zhu et al. 2012; Owen 2014).

Paardekooper & Mellema (2004) were the first to simulate dust gaps opened by low-mass planets, finding gaps opening at resonances. Their simulated ALMA images demonstrated the capability of ALMA to observe such structures: they found that a 0.05 M_J (15 $M_\oplus$) planet opens a gap in the dust while a 0.01 M_J (3 $M_\oplus$) does not, but do not elaborate further on the detectability threshold. In an extensive work, Zhu et al. (2014) showed that even a planet with a mass as little as 8 $M_\oplus$ can affect the dust surface density, creating a double-gapped structure. However, the observational consequences are not explored in this paper. Moreover, this work considers only inviscid discs and therefore cannot explore the effect of viscously driven inflow in the gas in modifying the resultant dust structures. Dong, Zhu & Whitney (2015) focused on giant planets and their impact on transitional discs, but they also simulate a 0.2 M_J planet which they find is able to open a gap in the dust. They also find that such a low-mass planet is not able to affect the spectral energy distribution. To the best of our knowledge, their work is the only one that, when exploring the observational consequences, is not restricted to ALMA wavelengths but also includes simulated NIR images. However, no study is made of systematically lowering the planet mass until the observed signatures disappear. In a series of papers, Fouchet, Gonzalez & Maddison (2010) explored the impact of planets on the dust distributions, but in creating synthetic ALMA observations (Gonzalez et al. 2012) only the gas giant regime is explored. Even more recently, the HL Tau observations (Brogan et al. 2015) prompted other works which have focused on explaining the ring structure that was observed. Dipierro et al. (2015) interpreted the image using three planets, finding a best fit with masses of 0.2, 0.27 and 0.55 M_J. Picogna & Kley (2015) also interpreted the HL Tau image in terms of planets, but in this case only two planets are invoked (with best-fitting masses 0.07 and 0.35 M_J). The authors also commented that, depending on the disc parameters, they find observable gaps even assuming masses of 10 and 20 $M_\oplus$. Finally, Jin et al. (2016) also interpreted the image using three planets, but with best-fitting masses of 0.35, 0.17 and 0.26 M_J.

The above works have shown convincingly that there is a prospect for observing low-mass planets in discs. However, as we have highlighted, no work so far has directly established what is the minimum planet mass that creates observable features at high resolution with current instruments (or those planned for the near future). In addition, most of the effort has concentrated on ALMA and very little attention has been dedicated to scattered light images, which however have the same resolution as ALMA. Finally, to the best of our knowledge, the literature contains no predictions of this kind for MIR thermal images; with the upcoming generation of 30 m class telescopes, images at these wavelengths will in a few years have the same resolution as existing submm and NIR instruments. The goal of this paper is to remedy this omission by deriving a threshold for the observability of a planetary gap in protoplanetary discs at NIR, MIR and submm wavelengths, as well as studying the dependence of this threshold on disc properties.

This paper is structured as follows. We present our method in Section 2 and the results from the multi-fluid simulations in Section 3. We then present the simulated observations in Section 4. Section 5 discusses our results and we draw our conclusions in Section 6.

2 NUMERICAL METHOD AND INITIAL CONDITIONS

Our methodology consists of running 2D multi-fluid gas dust simulations of planet–disc interactions. We then post-process the simulations by calculating synthetic observations at three different wavelengths (NIR, MIR and submm).

2.1 Gas and dust dynamics

We run 2D multi-fluid simulation where we evolve at the same time the dust and the gas using the FARGO-3D code (Benítez-Llambay et al. 2015). FARGO uses the ZEUS numerical algorithm (Stone & Norman 1992). The algorithm is well tested and it has been used many times for protoplanetary disc studies (see de Val-Borro et al. 2006 for an algorithmic comparison). We extended the code to include dust, approximating the dust as a pressureless fluid that is coupled to the gas via linear drag forces. We have neglected feedback from the dust on to the gas. These approximations are valid for low dust-to-gas ratios and particles with Stokes number (see the next paragraph) St < 1 (Garaud, Barrière-Fouchet & Lin 2004).

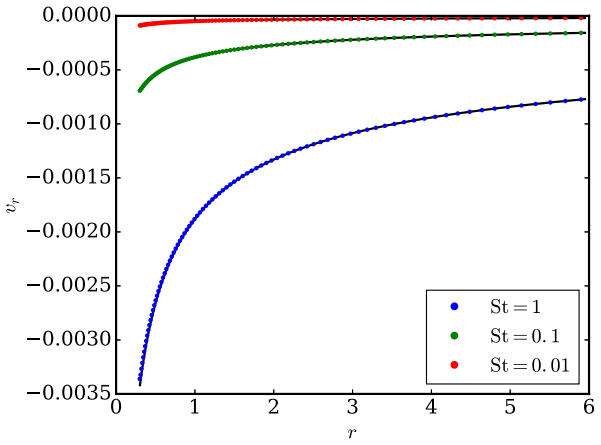

Figure 1. Radial velocity of the dust in a 2D disc for a range of Stokes numbers. The velocity from the simulation (points) agrees well with the analytical solution (solid lines; Takeuchi & Lin 2002).

The equation for the dust velocity, $\boldsymbol{v}_\mathrm{d}$, is given by

$$\frac{\mathrm{d}\boldsymbol{v}_\mathrm{d}}{\mathrm{d}t} + \boldsymbol{v}_\mathrm{d}\cdot\nabla\boldsymbol{v}_\mathrm{d} = -\frac{1}{t_\mathrm{s}}(\boldsymbol{v}_\mathrm{d} - \boldsymbol{v}_\mathrm{g}(t)) + \boldsymbol{a}_\mathrm{d}, \tag{1}$$

where $\boldsymbol{v}_\mathrm{g}$ is the gas velocity, $\boldsymbol{a}_\mathrm{d}$ are the non-drag accelerations felt by the dust and t_s is the stopping time. It is common to introduce the dimensionless stopping time, also called Stokes number, defined as $\mathrm{St} = t_\mathrm{s}\Omega_\mathrm{k}$, where Ω_k is the Keplerian angular velocity at the given location in the disc. We solve this equation along with the continuity equation $\frac{\partial\Sigma_\mathrm{d}}{\partial t} + \nabla\cdot(\Sigma_\mathrm{d}\boldsymbol{v}_\mathrm{d}) = 0$, using the ZEUS algorithm, in which the forces (source step, RHS of equation 1) are evaluated prior to the advection (transport step, $\boldsymbol{v}_\mathrm{d}\cdot\nabla\boldsymbol{v}_\mathrm{d}$ term). The transport step for the dust is identical to that of the gas. For details, see Stone & Norman (1992), Masset (2000) and references therein.

The source step for the dust is evaluated semi-implicitly, using the analytical solutions available for the simple form of the drag law. We take into account the change in gas velocity over the time step by approximating $\boldsymbol{v}_\mathrm{g}$ as $\boldsymbol{v}_\mathrm{g}(t') = \boldsymbol{v}_\mathrm{g}(t) + \boldsymbol{a}_\mathrm{g}\times(t'-t)$ throughout the time step, where $\boldsymbol{a}_\mathrm{g}$ is the acceleration calculated explicitly (that is, at time t) during the source step for the gas. The dust velocity at $t+\Delta t$ is given by

$$\begin{aligned}\boldsymbol{v}_\mathrm{d}(t+\Delta t) = {}& \boldsymbol{v}_\mathrm{d}(t)\exp(-\Delta t/t_\mathrm{s}) + \boldsymbol{a}_\mathrm{g}\Delta t \\ & + \left[\boldsymbol{v}_\mathrm{g}(t) + (\boldsymbol{a}_\mathrm{d} - \boldsymbol{a}_\mathrm{g})t_\mathrm{s}\right](1 - \exp(-\Delta t/t_\mathrm{s})),\end{aligned} \tag{2}$$

which reproduces the explicit update when $\Delta t \ll t_\mathrm{s}$ and the short friction time limit when $\Delta t \gg t_\mathrm{s}$. To see this, consider $\boldsymbol{a}_\mathrm{d} = \boldsymbol{g}$ and $\boldsymbol{a}_\mathrm{g} = -\frac{\nabla P}{\Sigma_\mathrm{g}} + \boldsymbol{g}$, where $\boldsymbol{g}$ is the gravitational acceleration and P is the gas pressure. For $\Delta t \gg t_\mathrm{s}$

$$\boldsymbol{v}_\mathrm{d}(t+\Delta t) \rightarrow \boldsymbol{v}_\mathrm{g}(t+\Delta t) + t_\mathrm{s}\frac{\nabla P}{\Sigma_\mathrm{g}}, \tag{3}$$

i.e. the short friction time limit.

The time step, Δt, is limited by both the time step of the gas and via a Courant-Friedrichs-Lewy (CFL)-like criterion for the dust, $\Delta t = C\Delta x/\max(|v_\mathrm{d}|, |v_\mathrm{d} - v_\mathrm{g}|)$, where we use a conservative value of $C = 0.44$ for both the gas and dust. We have verified the technique using a range of tests. For example, Fig. 1 shows that the code achieves good agreement between the radial velocity obtained in a low-resolution ($N_r \times N_\phi = 350 \times 580$) 2D simulation and the analytical solution (Takeuchi & Lin 2002).

Additionally, mass diffusion was added to the surface density in the dust using a Schmidt number $\mathrm{Sc} = 1$. The diffusive mass flux, $\boldsymbol{F}_\mathrm{D} = -(\nu/\mathrm{Sc})\Sigma_\mathrm{g}\nabla(\Sigma_\mathrm{D}/\Sigma_\mathrm{G})$, where ν is the turbulent viscosity (Clarke & Pringle 1988), was included by adding an effective diffusive velocity $\boldsymbol{v}_\mathrm{D} = \boldsymbol{F}_\mathbf{D}/\Sigma_\mathrm{D}$ to the velocity at which the dust is advected during the transport step.

2.2 Initial conditions and parameters

For the viscosity, we use the α prescription of Shakura & Sunyaev (1973) assuming $\alpha = 10^{-3}$. We use 2D cylindrical coordinates and dimensionless units in which the orbital radius of the planet (r_p) is at unity, the unit of mass is that of the central star, while the unit time is the inverse of the Kepler frequency of the planet. The inner radial boundary of our grid is at 0.5 r_p and the outer boundary at 3 r_p; we use non-reflecting boundary conditions at both boundaries. The resolution is 450 and 1024 uniformly spaced cells in the radial[1] and azimuthal direction, respectively. We let the disc relax for a time t_0 of 10 orbits before introducing the planet, and then, to avoid numerical artefacts, we increase the mass of the planet from zero to the final one over a time t_taper of 20 orbits, according to the formula $\sin^2(\pi/2\times(t-t_0)/t_\mathrm{taper})$. The planet is kept on a circular orbit whose orbital parameters are not allowed to vary. The surface density profile is given by

$$\Sigma(R) = \Sigma_0\frac{r_\mathrm{p}}{R}, \tag{4}$$

where the value of the normalization constant Σ_0 is arbitrary as far as the dynamics is concerned. In our fiducial model, the disc has an aspect ratio H/R at the location of the planet of 0.05. The aspect ratio varies in a power-law fashion with a flaring index of 0.25. The value of the aspect ratio is particularly important as it controls the strength of the pressure forces, which are responsible (see Section 3.1) for closing the planetary gap. For this reason, we also run models with a different value of the aspect ratio. We chose values of 0.025 ('cold') and 0.1 ('hot') that encompass the possible range of variation in real protoplanetary discs.

For the fiducial model, we run simulations with different planet masses, considering values of 8, 12, 20, 60, 120 $\mathrm{M}_\oplus$. Note that as far as the dynamics is concerned, only the ratio of the planet mass to the star mass matters; the planet masses we quote assume a central mass of 1 $\mathrm{M}_\odot$, and need to be properly rescaled with the star mass. When varying the aspect ratio of the disc, we also run models for additional values of the planet mass, as the aspect ratio controls how massive a planet must be to significantly affect the surface density of the disc. For the 'cold' disc case ($H/R = 0.025$), we also run models for a mass of 2.5 $\mathrm{M}_\oplus$, and for the 'hot' disc case for masses of 96, 160, 480 $\mathrm{M}_\oplus$.

Along with the gas dynamics, we integrate in time the evolution of the dust. To keep our simulations scale-free, we fix the Stokes number St of the grains rather than their physical size. Once the physical scales of the disc have been chosen, it is then possible to convert our Stokes numbers to real sizes as we explain in the next section. We use five dust sizes, with Stokes numbers (logarithmically spaced) ranging from 2×10^{-3} to 0.2.

2.3 Radiative transfer

To investigate the detectability of dust gaps opened by low-mass planets, we calculate images at various wavelengths using the 3D

[1] While this gives a different relative resolution across the grid, the limited range in radii of our grid does not make the effect significant.

radiative transfer code RADMC-3D.[2] In the radiative transfer calculation, we use a 3D spherical mesh with $N_r = 256$, $N_\theta = 180$, $N_\phi = 384$ grid points in the radial, poloidal and azimuthal direction, respectively. For the radial direction, we use a logarithmic grid extending from 1 to 100 au while an arithmetic grid is used for the angular coordinates. To ensure that we resolve the disc properly in the vertical direction, we place $N_\theta = \{10, 160, 10\}$ points in the $[0, \pi/2 - \theta_0]$, $[\pi/2 - \theta_0, \pi/2 + \theta_0]$, $[\pi/2 + \theta_0, \pi]$ intervals, respectively, where $\theta_0 = 5H/R$, H/R being the aspect ratio of the disc taken at the outer edge of the disc.

The disc density distribution for a given grain size a is assumed to be

$$\rho_a(R, z, \phi) = \frac{\Sigma_a(R, \phi)}{\sqrt{2\pi}H(R)} \exp\left(-\frac{z^2}{2h(R)^2}\right), \quad (5)$$

where $\Sigma_a(R, \phi)$ is the dust surface density, $R = r \sin\theta$ and $z = r\cos\theta$ and $H(R)$ is the pressure scaleheight. For the latter, we use the same value, as a function of radius, as is assumed in the hydrodynamic simulations. The dust surface density of the disc is taken from the hydrodynamic simulation in the following way. First, we take both the gas and dust surface density from the hydrodynamic simulations and bilinearly interpolate them to the spatial grid used in the radiative transfer calculations. We extrapolate the disc both inwards and outwards of the hydrodynamic computational domain[3] if it is necessary assuming that $\Sigma(R) \propto R^{-1}$. Then we calculate the gas density structure using equation (5). As our hydrodynamics simulations are not 3D, we did not include dust settling or iterated to reach hydrostatic equilibrium. Including these effects properly would require including also other 3D effects which are potentially more important, which goes beyond the scope of this paper (see the discussion in Section 5.3). Neglecting settling is particularly relevant for the submm dust; however, we note that, given that it is optically thin, observations mostly probe the dust surface density, and at submm wavelengths are not really sensitive to the details of the vertical structure. In addition, while settling might change the global temperature of the disc, this would result only in a global change of the surface brightness, whereas here we are interested in the substructure present in the image. The same argument can be applied to another inconsistency that stems from our approach, namely that the temperature assumed for the hydro calculation might be different from the one computed by RADMC-3D. Also, we remark that such inconsistencies always arise when using parametric models; the benefit is that they allow us to set up a controlled environment.

The dimensionless surface density provided by FARGO-3D is converted to dimensional form taking the planetary orbital radius to be 30 au and normalizing the density such that the gas mass in the disc is 0.01 $M_\odot$ within 100 au. The corresponding normalization of the gas surface density at 1 au is $\sim$300 g cm^{-2}. For what concerns the dust, we normalize the density so that the initial dust-to-gas ratio is 10^{-2}. We use 10 logarithmically spaced grain size bins between 0.1 μm and 1 mm and assume that the dust grain size distribution follows $\mathrm{d}N/\mathrm{d}a \propto a^{-3.5}$.

Then for a given dust grain size, we calculate the Stokes number in the disc mid-plane, assuming that the particles are in the Epstein regime:

$$\mathrm{St} = t_\mathrm{s}\Omega = \frac{a\rho_\mathrm{d}\Omega}{\rho_\mathrm{g}c_\mathrm{s}} = \frac{a\rho_\mathrm{d}}{\Sigma_\mathrm{g}}, \quad (6)$$

where a is the size of the particles, ρ_d is the bulk density of the dust, which we assume to be 3.6 g cm^{-3}, ρ_g is the density of the gas and Σ_g is the surface density of the gas. To arrive at the last expression, we have used the fact that $\Sigma_\mathrm{g} = \rho_\mathrm{g}H$ and $H = c_\mathrm{s}/\Omega$; note that in these equations we have neglected factors of order unity. At any given location in the disc, we perform a linear interpolation in Stokes number to compute the dust surface density, starting from the results of our hydrodynamical simulations. When the Stokes number is smaller than the smallest one we have in the multi-fluid simulation, we assume that the dust follows the gas. We note that with our parameters the typical Stokes number of 1 mm particles at 30 au is $\sim$0.07 and $\sim$0.17 at 100 au, which ensures that we have enough information from the multi-fluid simulations to reconstruct the surface density of those particles.

The mass absorption coefficients of the dust grains are calculated with Mie theory using the optical constants of astronomical silicates (Weingartner & Draine 2001). The radiation field of the central star is modelled with blackbody emission and the star is assumed to have parameters, typical for a Herbig Ae star,[4] $M_\star = 2\ M_\odot$, $T_\mathrm{eff} = 9500$ K, $R_\star = 2.5\ R_\odot$.

As a first step, we calculate the temperature of the dust with a thermal Monte Carlo simulation, then we calculate images at 1.65, 10 and 880 μm taking the disc inclination to be 10°. We use 1.6×10^8 and 9×10^7 photons for the thermal Monte Carlo simulations and for the image calculations, respectively.

3 RESULTS FROM THE GAS AND DUST DYNAMICS SIMULATION

3.1 Gas surface density

We find that it is necessary to integrate for a relatively long time to reach a consistent steady state. We show the time evolution of the surface density for a representative case of 60 $M_\oplus$ in Fig. 2. Different lines correspond to different snapshots from the simulations: 150 orbits (blue dotted line), 400 orbits (green dot–dashed line), 1000 orbits (red dashed line) and finally 3000 orbits (solid cyan line). While the gas converges reasonably close to the final result on a time-scale of $\simeq$100 planetary orbits, the depth of the gap still slowly evolves over a time-scale of $\simeq 10^3$ planetary orbits, over which the depth typically changes by a factor of <2. This result is consistent with what other authors have found previously when looking at the time-scale of gap opening (Varnière, Quillen & Frank 2004; Duffell & MacFadyen 2013; Fung, Shi & Chiang 2014) and can be understood in terms of the time-scale to reach gap opening being roughly the viscous time-scale across the gap. For reference, if we assume that the perturbed region has a width Δ of few scaleheights: $\Delta = xH$ (with x a constant with a value of a few), we find that the time-scale for gap opening is $x^2/(2\pi\alpha) \sim 150x^2$ orbits.

[2] http://www.ita.uni-heidelberg.de/dullemond/software/radmc-3d/

[3] In particular, we do not consider the first six cells of hydrodynamical computational domain, which are affected by the inner boundary condition and show an artificial dust accumulation.

[4] The spectral type and luminosity of the central star (e.g. HAe versus TTs) affect only the absolute surface brightness of the disc but do not influence the morphology of the images. The choice of using a Herbig Ae stellar model is motivated by the fact that most of the sources observed by current instruments in the NIR like SPHERE or GPI are Herbig Ae stars due to sensitivity limitations.

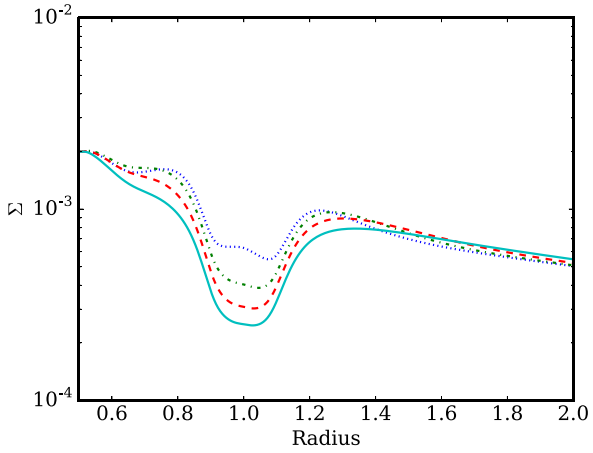

Figure 2. Azimuthally averaged gas surface density for the fiducial model for a planet mass of 60 $M_\oplus$. Different lines correspond to different snapshots from the simulations: 150 orbits (blue dotted line), 400 orbits (green dot–dashed line), 1000 orbits (red dashed line) and finally 3000 orbits (solid cyan line).

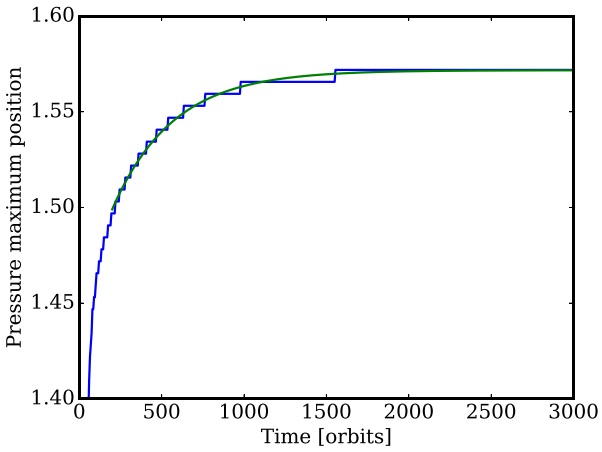

Figure 3. Evolution with time of the location of the pressure maximum outside the planet orbit (blue line) for the reference case of 480 $M_\oplus$ in the 'hot' disc. We also fit the data with an exponential (green line) to show that convergence has been reached.

Crida et al. (2006) found that instead the relative surface density profile, i.e. $(1/\Sigma)(\mathrm{d}\Sigma/\mathrm{d}r)$, is established on a much faster time-scale.

While the gas evolution has few observational implications in itself, we find that the dust can change more significantly over this time-scale. In particular, the dust is sensitive to the pressure profile of the gas. If the planet is massive enough, it creates a pressure maximum in the gas that will trap dust (Rice et al. 2006), as we detail in Section 3.3. The location of this maximum has therefore a deep impact on the dust structure and we find that it reaches convergence after the stated time interval. We show in Fig. 3 the evolution with time of the location of the pressure maximum for an illustrative case of a planet of 480 $M_\oplus$ in the 'hot' disc, that is, $H/R = 0.1$. We choose this disc because the viscous time-scale in this disc is faster than for the other aspect ratios, which allows us to explore more the evolution in time of the pressure maximum. The curve (blue line) can be fitted with an exponential (green line) with a tapering time-scale of ∼370 orbits; the value that the exponential tends to is almost indistinguishable from the value after 3000 orbits.

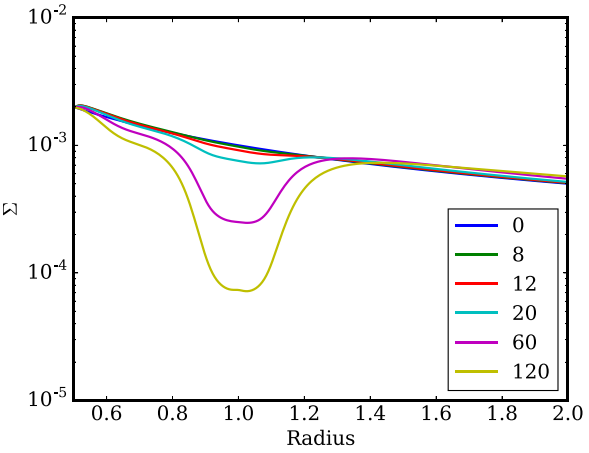

Figure 4. Azimuthally averaged gas surface density for the fiducial model for the different planet masses.

For the fiducial model, an exponential convergence is not so clear and the curve can be fitted equally well by a logarithm. Assuming that we can rescale the time-scale with $(H/R)^2$, we can estimate the error in the location of the pressure maximum in the fiducial model that is introduced by only running for 3000 orbits to be 0.2 H, by estimating the error for the 'hot' case if we had stopped after 750 orbits. Even for the 'cold' case, the error is less than H. We remark that current observational facilities are not able to resolve a scaleheight in discs at a distance of 30 au from the star, so that our estimates are accurate enough for observational applications. In what follows, we choose then to present our results after 3000 orbits.

Fig. 4 shows the azimuthally averaged surface density of the gas for the fiducial model after 3000 planetary orbits. In this figure, it can be seen that there is little modification to the gas surface density for the least massive cases. The 120 $M_\oplus$ planet produces a gap that involves a reduction in surface density by a factor of 10; the 60 $M_\oplus$ one produces a partial gap that involves a reduction by a factor of 4. The relatively small depth of these gaps is not surprising given that for the planet masses considered here only the most massive case is in the gap opening regime. Two commonly used (Lin & Papaloizou 1993) criteria for gap opening are the so-called thermal criterion, according to which the planet Hill radius R_H must be greater than the vertical scaleheight of the disc H:

$$q \gtrsim 3\left(\frac{H}{R}\right)^3, \tag{7}$$

where $q = M_\mathrm{pl}/M_*$ (we assume $M_* = 1\,M_\odot$ for simplicity in what follows), and the viscous criterion, according to which the time-scale to open the gap must be smaller than the time-scale for viscosity to close it:

$$q \gtrsim \left(\frac{27\pi}{8}\right)^{1/2}\left(\frac{H}{R}\right)^{5/2}\alpha^{1/2}. \tag{8}$$

Substituting numerical values for our case gives a threshold mass ratio of $4 \times 10^{-4} \simeq 120\,M_\oplus$ for the thermal criterion and $5.5 \times 10^{-5} \simeq 16\,M_\oplus$ for the viscous criterion. This means that for our choice of parameters the pressure forces are the dominant ones trying to close the gap and therefore only the thermal criterion should be considered. To be in the regime where also viscosity is important would require to consider a lower value of H/R or a bigger value of α. Note that however, due to the shallow dependence on α and the similar dependence on H/R, in practice this happens only for quite

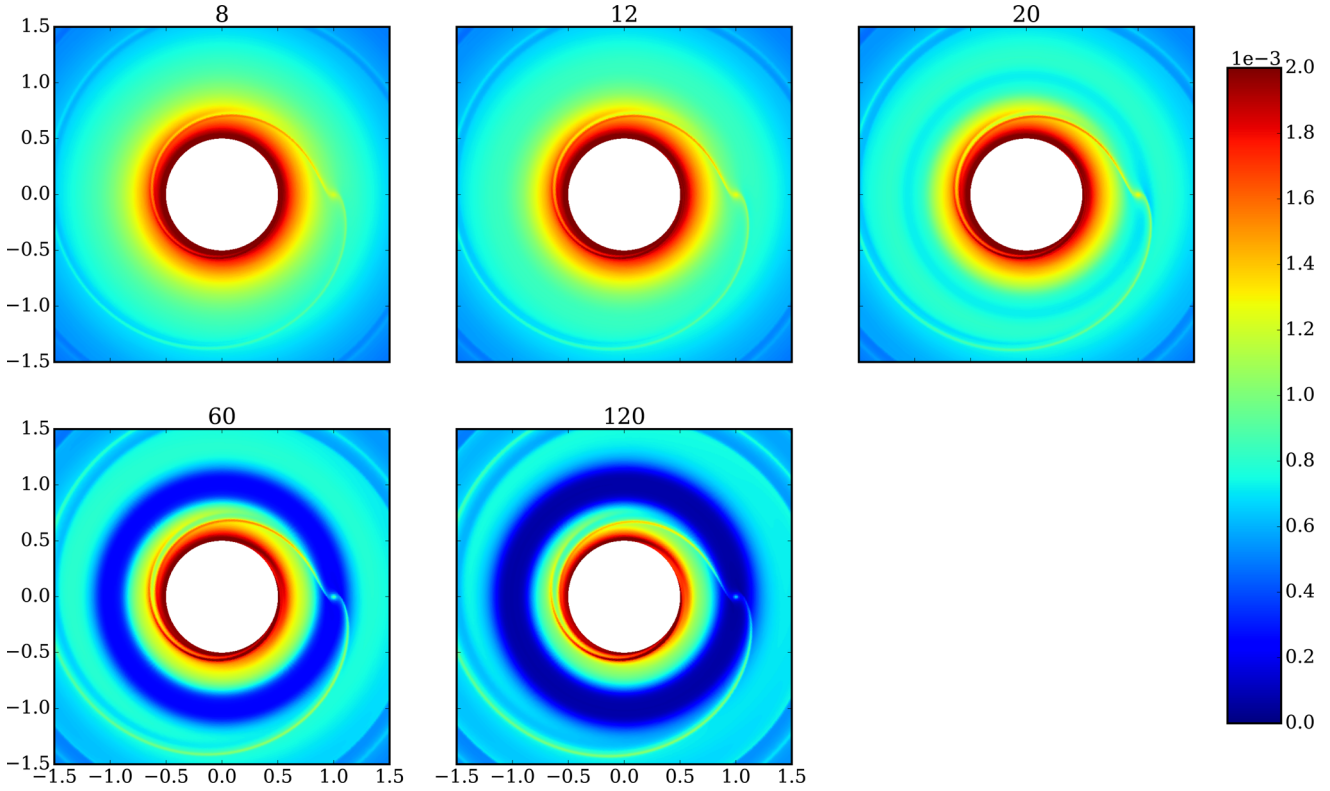

Figure 5. Gas surface density for the different planet masses (as indicated in Earth masses).

extreme values of the parameters. Crida et al. (2006) collected the two criteria in only one that accounts for both conditions:

$$\frac{3}{4}\frac{H}{R_{\rm H}} + \frac{50\nu}{q r_{\rm p}^2 \Omega_{\rm p}} \lesssim 1. \quad (9)$$

The interested reader can consult Baruteau et al. (2014) for an alternative formulation of the same criterion, which gives explicitly the mass ratio q. The numerical factors in this equation are slightly different so that the threshold mass ratio is approximately $1.5 \times 10^{-4} \simeq 45\,{\rm M}_\oplus$. However, note that their definition of gap is a factor of 10 reduction in the surface density, which actually happens in our simulations only for the most massive planet. Simplified criteria like the ones we quote here can be used only as order-of-magnitude estimates and one should not overinterpret them. What matters for the purpose of this paper is that these planets are not in a regime where they open deep gaps in the gas surface density such as those opened by Jupiter-mass planets. Finally, note the very steep dependence of the thermal criterion on the disc temperature, which will be important in the rest of the paper.

Fig. 5 shows the 2D gas surface density. Note that although the gap starts to be visible only for the $60\,{\rm M}_\oplus$ case, all planets generate a clear spiral in the 2D gas surface density. Such spirals however are too thin and with a contrast that is too low to be observed. We will show this in the next section where we show simulated observations. Even in the case of very massive planets, the conclusions of Juhász et al. (2015) were that it is extremely hard to detect spirals such as the ones recently imaged in the scattered light (e.g. Muto et al. 2012; Garufi et al. 2013; Benisty et al. 2015; Wagner et al. 2015). It should therefore not be surprising that spirals are not detectable for these low-mass planets.

3.2 Dust surface density

We begin by reporting the features produced in the dust by planets of varying mass; the observability of these features will be discussed in Section 4. It is impossible to show all the results from our simulations in the limited space of this paper. Instead, it is more instructive to understand the trends with planet mass and particle size and to determine what drives this behaviour. As a representative example, we show for a $20\,{\rm M}_\oplus$ planet how the dust surface density varies with Stokes number (Fig. 6).[5] For sufficiently small dust particles, which are well coupled to the gas, the depth of the gap in the dust density should be the same as the gas. For our smallest size, we indeed see only slight difference between dust and the gas; however, it is possible to see that the dust density at the edge of the gap is slightly larger. By the next size we simulate (St = 0.063), there is already an order unity variation in the surface density, which continues to increase with increasing dust size.

From these images, it is clear that the structures in the dust density are largely azimuthally symmetric (for the planet masses we consider here; for massive enough planets this is not necessarily true), with the exception of the spiral feature, which is thin and only has a small density enhancement associated with it. Thus, it is instructive to consider the trends seen in azimuthally averaged profiles. From the azimuthally averaged profiles (Figs 7 and 8), we see that increasing both the planet mass and particle size leads to stronger effects in the dust. The trends with planet mass for a fixed Stokes number (here St = 0.02, Fig. 7) show that the depth of the

[5] Note that the multi-fluid simulations are not sensitive to the normalization of the dust surface density; for illustrative purposes in Figs 6–8, we have normalized each dust surface density so that it has initially the same value as the gas surface density.

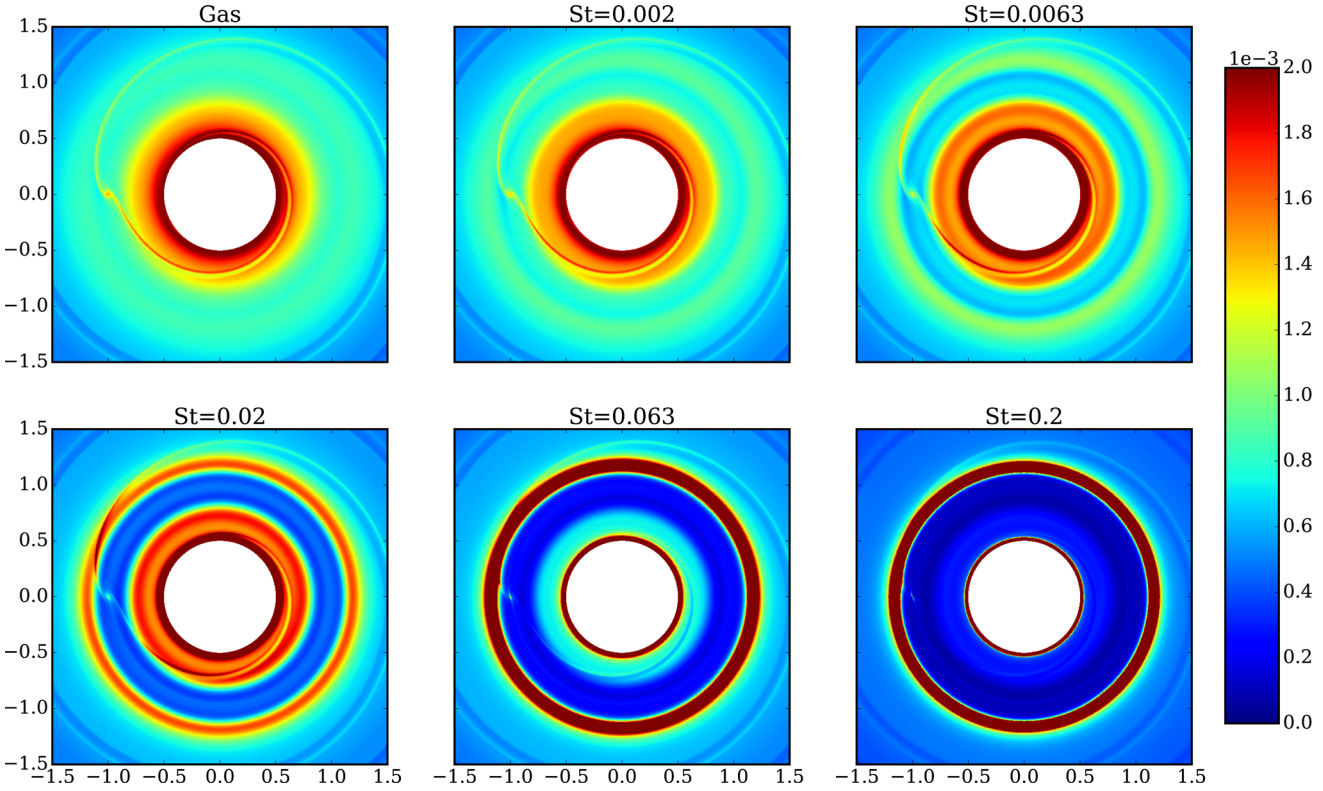

Figure 6. Dust surface density for the 20 $M_\oplus$ planet. Different panels correspond to different Stokes numbers as shown in the legend. For reference, we show also the gas surface density.

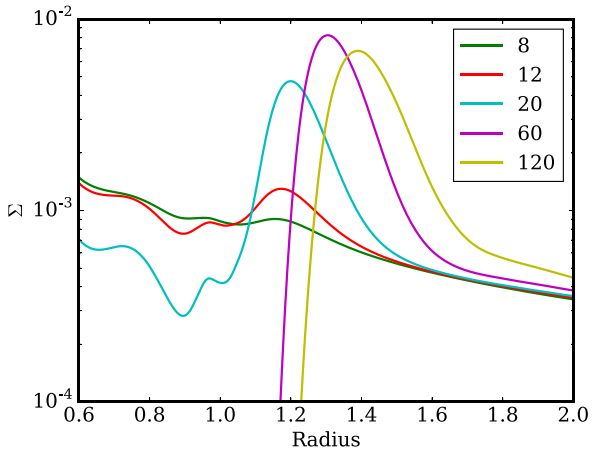

Figure 7. Dust surface density with St = 0.02 for the different planet masses.

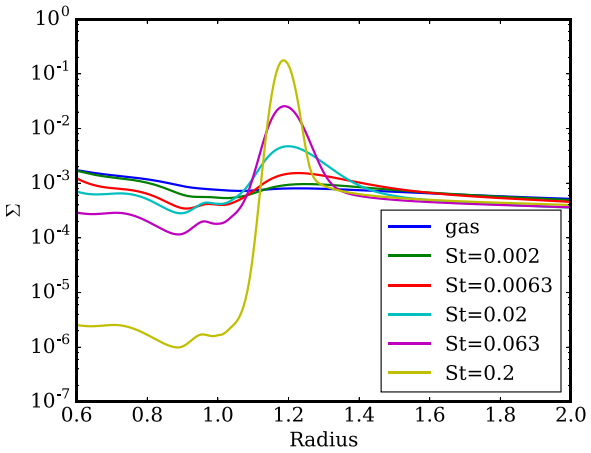

Figure 8. Dust surface density for the 20 $M_\oplus$ planet. Different lines correspond to different Stokes numbers as shown in the legend. For reference, we show also the gas surface density.

gap depends clearly on the planet mass, with more massive planets creating deeper gaps. The 8 $M_\oplus$ planet does not significantly modify the dust surface density (the variation is only a few per cent even for the largest dust size we simulate), while the 12 $M_\oplus$ produces variations of order unity. The 60 and 120 $M_\oplus$ planets actually create a *hole* rather than a narrow *gap*, meaning that the surface density of the dust inside ∼1.2 times the orbital radius of the planet is severely depleted of dust; the 20 $M_\oplus$ planet is in between a gap and a hole. There is thus only a limited range of planet masses that create detectable gaps for this Stokes number; planets that are massive enough will eventually form holes. Similar trends hold with particle size, with the 20 $M_\oplus$ planet opening a gap in the St = 0.2 dust. One notable fact is that while the location of the peak dust density in the ring depends on planet mass, it is not a function of grain size.

Even for planets that just open gaps, we find that the gaps opened in dust can be much deeper than the ones in the gas, consistent with what was found by previous authors (Paardekooper & Mellema 2006; Zhu et al. 2014). Compare for example the 20 $M_\oplus$ case in Fig. 7 with Fig. 4, where the presence of a planet is only barely visible by looking at the surface density. In addition, the more massive cases we simulate not only show a gap or a hole, but also a bright ring in the surface density outside the orbital location of the

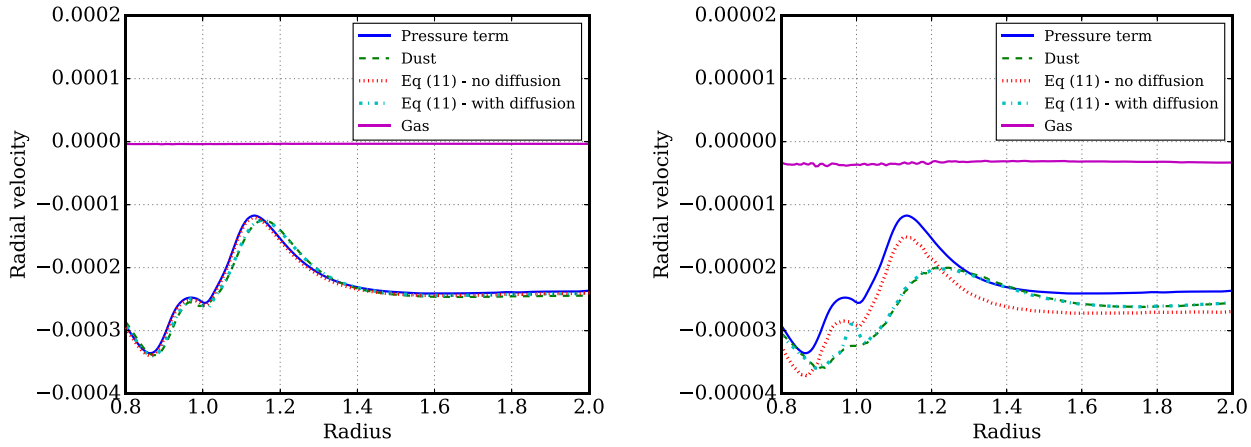

Figure 9. Dissection of the dust radial velocity for two sizes for the 12 $M_\oplus$ planet. The plots show the pressure gradient term from equation (11) (solid blue line), the actual value of the velocity from the simulation (dashed green line), the estimate of equation (11) with (dot–dashed cyan line) and without (dotted red line) the diffusion term and finally the gas radial velocity from the simulation (solid purple line). Left-hand panel: St = 0.07. Right-hand panel: St = 0.007.

planet. The enhancement of this peak, and even more interestingly its location, depends on the planet mass (Fig. 7). We will investigate the reasons for this morphology in Section 3.3. We do not find any feature like the one that Paardekooper & Mellema (2006) found at outer resonances, in line with the results of Zhu et al. (2014).

3.3 Dust radial velocity

Since the dust density is azimuthally symmetric, this suggests that the dust dynamics and resulting surface density can be understood in terms of a one-dimensional model in which the continuity equation is just

$$\frac{\partial \Sigma_{\rm d}}{\partial t} + \frac{\partial (R \Sigma_{\rm d} v_{\rm d,R})}{\partial R} = 0. \quad (10)$$

This equation can be closed with the knowledge of dust velocity; for particles with St $\ll 1$, we can make use of the short friction time approximation in which the dust velocity is given by

$$v_{\rm d} = v_{\rm g} + t_{\rm s} \frac{\nabla P}{\rho} + v_{\rm D}, \quad (11)$$

where the last term takes into account the diffusive flux. The expression provides a simple way of dissecting the dust velocity into the contribution from the gas and that due to the pressure gradient, since apart from at the gap edge $v_{\rm D}$ is generally small. Thus, the pressure term is responsible for the differences between the dust and the gas velocities; in turn, these affect the surface densities. It is straightforward to realize looking at the expression that the importance of the pressure gradient increases with the particle size.

Fig. 9 shows a comparison of the actual dust radial velocity from the simulation, azimuthally averaged, with the approximation given by equation (11) (where again quantities have been azimuthally averaged) for two dust sizes for the 12 $M_\oplus$ planet (left-hand panel: St = 0.07; right-hand panel: St = 0.007). Specifically, the plots show the pressure gradient term from equation (11) (solid blue line), the actual value of the velocity from the simulation (dashed green line), the estimate of equation (11) including (dot–dashed cyan line) or not (dotted red line) the dust diffusion term (that is, $v_{\rm D}$) and finally the gas radial velocity from the simulation (solid purple line). We can see that the pressure gradient is always negative. To state it in another way, the planet is not massive enough to create a pressure maximum outside the gap edge. Since this condition is required to trap dust particles (because it provides a location where the dust

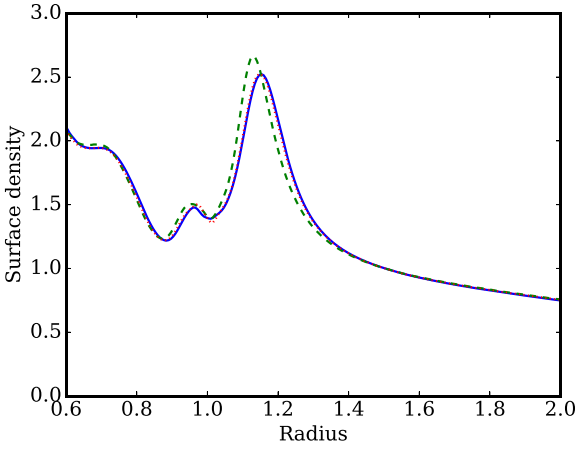

Figure 10. Comparison between the steady-state surface density predicted by equation (10) (green dashed line: without including dust diffusion; dotted red line: including dust diffusion) and the actual value from the simulation (solid blue line) for the 12 $M_\oplus$ planet, St = 0.07.

radial velocity is zero), the planet is unable to trap dust and open up a *hole* (Rice et al. 2006). However, there is still a region where the pressure gradient is weaker, resulting in a smaller radial velocity. This is then a 'traffic jam' rather than a dust trap, in which a higher dust density region is associated with the lower velocity. We conclude then that the existence of a pressure maximum is not a necessary condition to affect the dust surface density. While this paper was being refereed, Dipierro et al. (2016) proposed another mechanism that can open gaps in the dust without requiring a pressure maximum. We note that their mechanism is different from the one we describe here and applies to grains with a larger Stokes number (they assume St = 10).

We now illustrate that the dust is in (or close to) steady state. By setting $\partial \Sigma_{\rm d}/\partial t = 0$, the continuity equation reduces to $\Sigma \propto 1/(R v_{\rm R})$, from which the constant of proportionality can be fixed using the surface density far from the planet.

We demonstrate this in Fig. 10, which shows a comparison between the steady state expected from the continuity equation and the actual surface density from the simulation (solid blue line). We show two different steady-state predictions; the difference between them is that the dashed green line neglects dust diffusion (i.e. it is

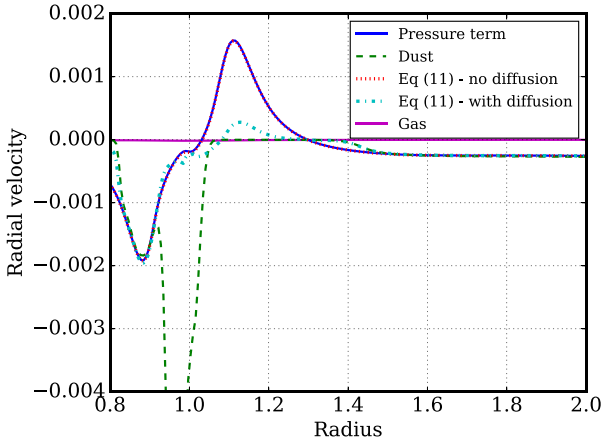

Figure 11. Dissection of the dust radial velocity for the 60 $M_\oplus$ planet (see Fig. 9 for the meaning of the different lines), St = 0.07.

computed using the dotted red line of Fig. 9), whereas the dotted red line includes it (i.e. it is computed using the dot–dashed cyan line). The remarkable agreement confirms that the structure that we see in the surface density is sculpted by the structure in the velocity, namely by (mostly) the pressure gradient (with a minor contribution from diffusion). This also means that in this particular case we could potentially have deduced the dust structure (neglecting dust diffusion) purely from the gas surface density and radial velocity, without running any multi-fluid simulation. However, for the right-hand panel of Fig. 9 (St = 0.007), dust diffusion is very important in smoothing out the structures carved by the pressure gradient. In this case, since the dust diffusion depends on the dust density, multi-fluid simulations are needed.

For more massive planets, the planet creates a maximum in the pressure and we have an actual pressure trap for large enough particles. We show in Fig. 11 one such case with a 60 $M_\oplus$ planet[6] and St = 0.07 dust, where the meaning of the lines is the same as in Fig. 9. For this particular size, the pressure gradient term is much larger than the gas velocity; however, the t_s dependence of this term (equation 11) means that there is a minimum dust size that can be trapped, which for a 60 $M_\oplus$ planet requires $\mathrm{St} \lesssim 3 \times 10^{-4}$. Particles above this size can only break through this trap via diffusion; thus, as noted by previous authors (Rice et al. 2006; Pinilla, Benisty & Birnstiel 2012b; Zhu et al. 2012), dust will continue to pile up at the location where the pressure gradient vanishes and a maximum in the dust surface density will occur. We will comment more on the location of the maximum in the dust in Section 5.1. Diffusion smooths out the maximum as it tends to cancel gradients in the dust concentration, so that the surface density will not grow indefinitely at the location of the pressure maximum. However, this takes a long time as reaching a steady state requires the diffusive velocity to be comparable to the pressure gradient term, and therefore a very big dust accumulation, which is provided by dust drifting from the outer part of the disc. Indeed, in our simulation we see that, for planets that create traps, the surface density at the pressure maximum is still increasing even after 3000 orbits, and no steady state has been reached yet (differently from the 'traffic jam' case shown previously). As shown in the previous section, the trap cuts out most of the supply to the inner disc, so that the planet opens a hole rather than a gap for this particular case (which for dust sizes close to the minimum hole opening size can be partially filled by diffusion). Fig. 11 also shows how the estimate provided by equation (11) breaks down close to the planet. Our interpretation is that 2D effects in this region cannot be neglected. In this case, only 2D dust dynamics simulations can recover the correct result.

We have repeated the same analysis shown here also for the 'cold' and 'hot' disc and confirm that a pressure maximum appears for the same ratio of the planet mass to thermal gap opening mass. To summarize, in our simulations the existence of a pressure maximum happens at a mass $\gtrsim 0.2 M_{\rm th} \sim 20((H/R)/0.05)^3\,M_\oplus$, where $M_{\rm th}$ is gap opening mass given by the thermal criterion. We then confirm the results of Lambrechts, Johansen & Morbidelli (2014), who in a different context found roughly the same value through 3D simulations. The fact that 2D and 3D simulations give a very similar result is very encouraging and means that this result can be taken to be robust.

4 SIMULATED OBSERVATIONS

To study the observability of the gaps, we also calculate simulated observations at NIR, MIR and submm wavelengths. In the NIR, we study the observability of the gaps with the current state-of-the-art imaging instrument, SPHERE on VLT (Beuzit et al. 2008). While the resolution of the currently available MIR instruments is too low to allow the detection of planets in this mass regime, this will change in a few years with the advent of 30 m class telescopes. We thus compute also MIR images, with the resolution of the planned NIR/MIR instrument, Mid-infrared E-ELT Imager and Spectrograph (METIS) on the E-ELT, to assess the potential of this wavelength in detecting low-mass planets. Since both of these instruments provide diffraction-limited resolution due to the extreme adaptive optics used, we simulate the observations by convolving the resulting images with a 2D Gaussian kernel. The full width at half-maximum (FWHM) was taken to be λ/D, where λ is the wavelength of observation and D is the telescope diameter.

In the case of the submm images, we simulate images using the Common Astronomy Software Applications[7] (CASA) v4.2.2. We use the `simobserve` task to simulate the observed visibilities and then the images are calculated from the visibilities using the `clean` task. The full 12 m array is used in two different configurations resulting in 0.027 and 0.091 arcsec resolution, respectively, at 880 μm. The source declination is taken to be $\delta = -25°$. We simulate observations with 1 h integration time using the full 7.5 GHz bandwidth and 0.913 mm precipitable water vapour, typical for band 7 observations. For all simulated observations, we assume that the distance to the source is 140 pc.

4.1 Fiducial model

Figs 12–14 show the simulated observations respectively for ALMA wavelengths (870 μm in band 7), in the NIR and in the MIR. It is clear how the presence of a gap is readily detectable in some of these images, despite the relatively low mass of the planet. Not only the gap itself, but also the bright ring outside the gap edge contributes in making the gap stand out visually. The comparison between the different ALMA resolutions allows us to establish what is the spatial resolution that allows us to reach the 'intrinsic' boundary posed by the fact that a minimum planet mass is required to significantly

[6] The 20 $M_\oplus$ planet also creates a pressure maximum, although only very shallow.

[7] http://casa.nrao.edu/index.shtml

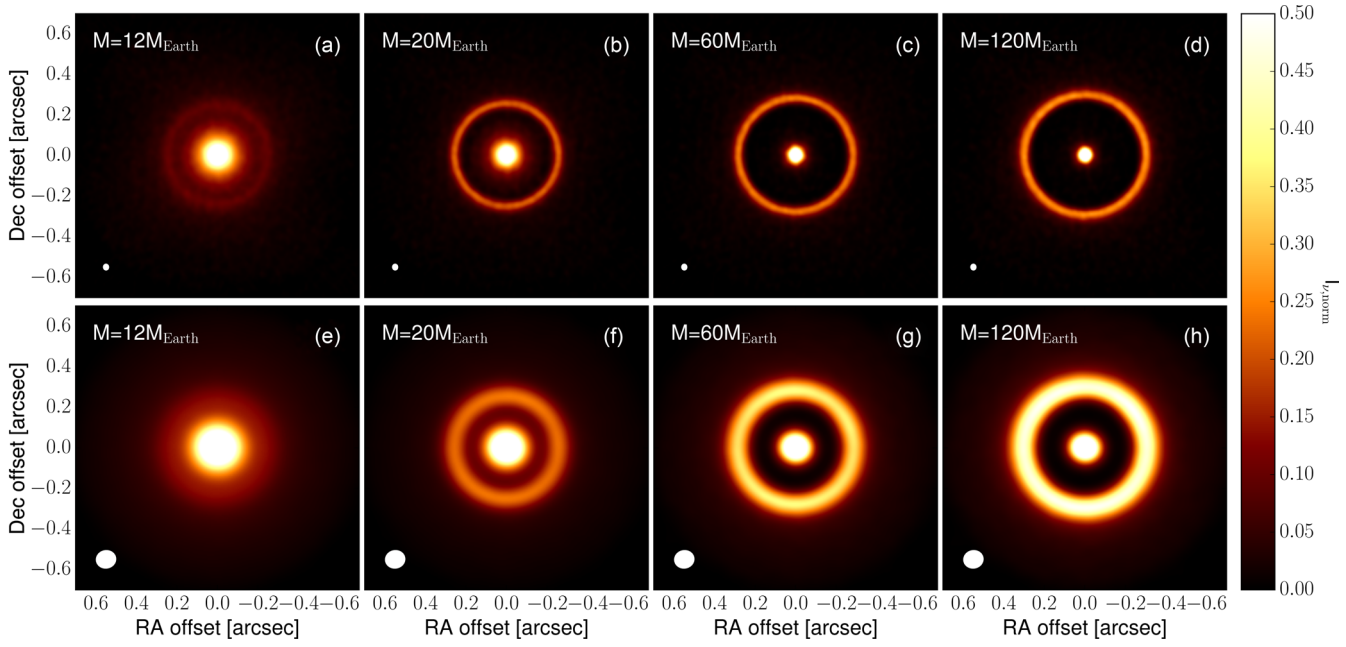

Figure 12. Submm images for four different planet masses for the fiducial model. We show two different resolutions of 0.025 arcsec (top row) and 0.091 arcsec (bottom row). The size of the synthesized beam is shown as a filled white ellipse in the bottom-left corner of each panel.

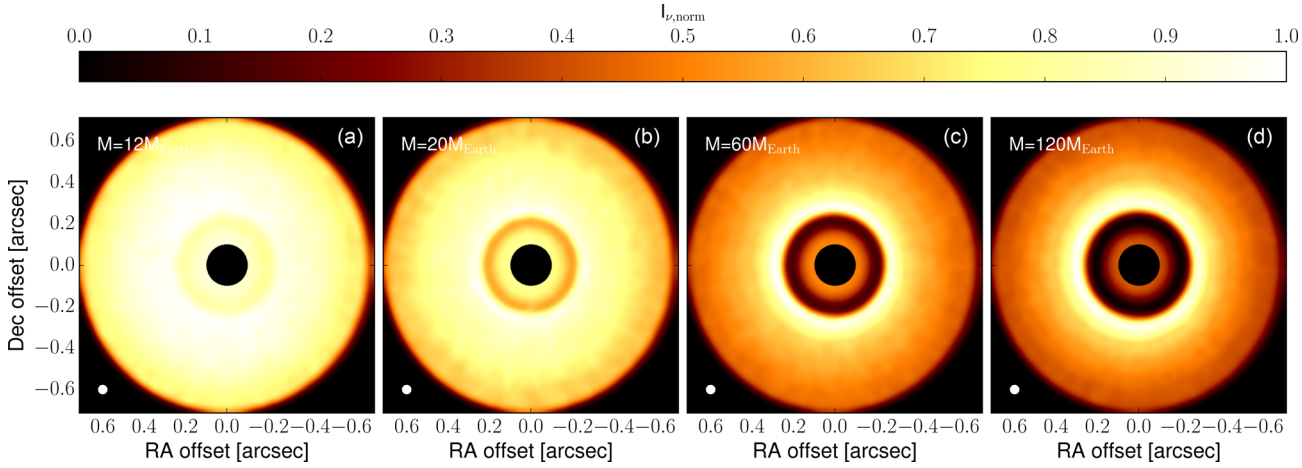

Figure 13. Images in the scattered light for the same planet masses as the previous figure. The resolution of the radiative transfer images was degraded to that of SPHERE on VLT (0.04 arcsec), by convolving the images with a 2D Gaussian kernel. The central 0.1 arcsec of the disc was masked to simulate the effect of a coronagraph. The images are scaled with the square of the radial distance from the central star. The size of the PSF is shown in the bottom-left corner as a filled white ellipse.

perturb the surface density of the disc. The 12 $M_\oplus$ planet is observable at the best resolution of 0.027 arcsec (corresponding to slightly more than 2 scaleheights), but not when the resolution is degraded to 0.091 arcsec. We also note that submm observations have a slight advantage over that of scattered light imaging when it comes to detecting the signature of a low-mass planet. The 12 $M_\oplus$ planet, while still visible with the highest angular resolution available to ALMA, is impossible to detect in the scattered light images. We interpret this phenomenon as due to the fact that the submm traces larger particles which are less coupled to the gas surface density. As noted in Section 3.2, this means that the gap is more pronounced for the large particles. This result is consistent with what other authors have found (Dong et al. 2015). For what concerns the MIR, we note that the results are largely similar to the NIR scattered light. While the MIR traces slightly larger particles, the difference is not significant enough to affect the images. Therefore, the minimum mass of a planet that can be detected through a gap in the dust image is wavelength dependent. In the submm, we can almost go down to 10 $M_\oplus$, while in the NIR and MIR (when it will become possible in the future) we are constrained to slightly larger masses of $\sim$20 $M_\oplus$.

4.2 Varying the aspect ratio

When we change the disc aspect ratio, the gap opening mass changes (equation 7). We might therefore expect that a simulation at a given H/R and planet mass should be 'equivalent' in terms of observability to one with another H/R value and a planet mass scaled according to $(H/R)^3$. This is however not entirely true because the overall spatial scale of the induced structure scales with H. Given finite instrumental resolution, this means that in cold discs the minimum

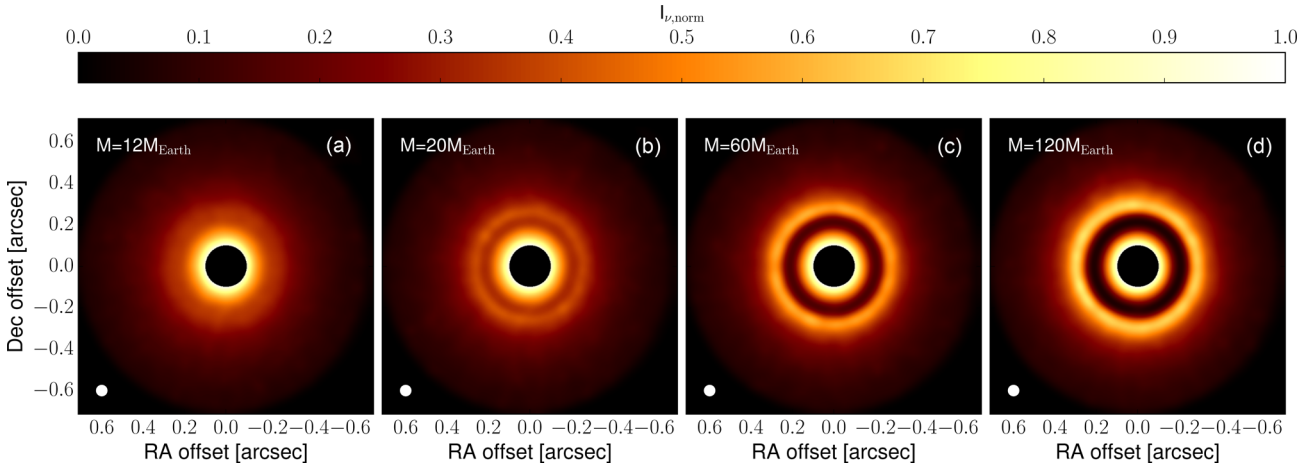

Figure 14. Images in the MIR of the thermal emission from the disc for the same planet masses as in Fig. 12. The resolution of the radiative transfer images was degraded to that of the future METIS instrument on the E-ELT by convolving the images with a 2D Gaussian with an FWHM of 0.05 arcsec. The images are scaled with the square of the radial distance from the star and the central 0.1 arcsec of the disc was masked to simulate the effect of a coronagraph. The size of the PSF is shown in the bottom-left corner as a filled white ellipse. Current instruments lack the spatial resolution to be able to resolve the morphologies we describe in this paper.

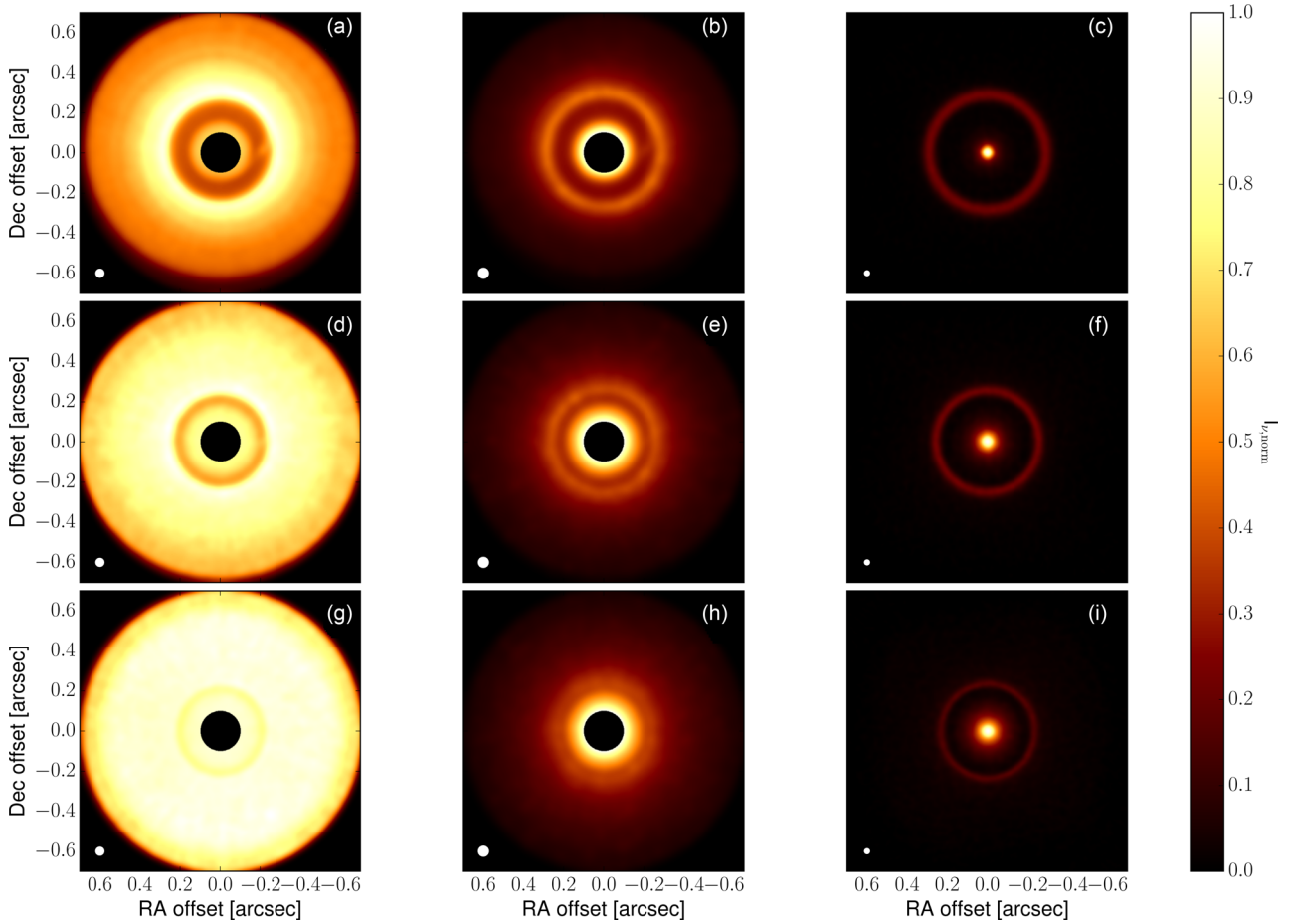

Figure 15. An example of how the aspect ratio of the disc changes the morphology of the image. We show the results for a planet mass of 20 $M_\oplus$, which corresponds to 2.5 $M_\oplus$ for the 'cold' disc and to 160 $M_\oplus$ for the 'hot' disc once the planet mass has been rescaled to have the same $M_{\mathrm{pl}}/M_{\mathrm{gap}}$ ratio. The top row is the 'hot' disc, the middle row is the fiducial model and the bottom row is the 'cold' disc. The columns show different instruments: SPHERE (left), METIS (middle) and ALMA (right). In the left and middle column, the images are scaled with the square of the radial distance from the star and central 0.1 arcsec of the disc was masked to simulate the effect of a coronagraph. The size of the PSF/synthesized beam is shown in the bottom-left corner as a filled white ellipse.

detectable planet mass does not decrease as steeply with H/R as the cubic dependence suggested by the simple argument above. This is illustrated in Fig. 15 where we show simulated observations for the three H/R values we simulate (0.025, 0.05 and 0.1) and planet masses which represent the same ratio of $M_{\rm pl}/M_{\rm gap}$ (that is, 20 $M_\oplus$ for $H/R = 0.05$, 2.5 $M_\oplus$ for the 'cold' disc and 160 $M_\oplus$ for the 'hot' disc). Although the simulations produce comparable depths of gaps in the gas, the very narrow feature produced by the lowest mass planet in the coldest disc is clearly the most challenging to detect observationally.

Thus, the detectability of the gap opened by a planet depends on two factors, the amount of depletion within the gap and the width of the gap. If the resolution of the observations is much higher [i.e. the size of the point spread function (PSF)/synthesized beam is much smaller than the width of the gap], the detectability of the gap depends only on the S/N of the image (i.e. whether or not the given amount of depletion in the gap could be robustly measured above the noise level). If, on the other hand, the width of the gap is comparable to or smaller than the size of the PSF/synthesized beam, the contrast between the gap and the surrounding disc is reduced, making the detectability of the gap more difficult. Indeed, this is the case in the 'cold' disc for the 2.5 $M_\oplus$ planet, which creates a gap that is narrower than the PSF.

5 DISCUSSION

5.1 Can we measure the planet mass?

Supposing that a real disc with the observed morphology described in this paper is found, a very important question is whether it is possible to measure the mass of the putative planet responsible for dust gap opening. As mentioned in Section 2.2, all the planet masses we quote in this section assume a central star of 1 $M_\odot$, and need to be rescaled properly with the stellar mass. Actually, this is also the case with the radial velocity method for detecting exoplanets after the protoplanetary disc has been dispersed. It highlights the importance of characterizing precisely the stellar parameters (e.g. Ligi et al. 2012, 2016). We have shown that in low-mass planet regime described in this paper we do not find any evidence for non-axisymmetric structures. This is in contrast to more massive planets that create vortices if the disc has a sufficiently low viscosity (Regály et al. 2012), an explanation that has been proposed for the asymmetries observed in transition discs.

In terms of *qualitative* differences, thus, the only one present in the cases discussed in this paper is the difference between gaps and holes in the submm dust. The presence of a hole in the submm dust points to a planet mass $\gtrsim$20 $M_\oplus$ for the fiducial model ($H/R = 0.05$). We can then conclude that the existence of a hole in the submm points to a planet mass $\gtrsim 0.2 M_{\rm th} \sim 20((H/R)/0.05)^3\,M_\oplus$, which corresponds to the minimum mass for which there is a pressure maximum in the gas. The opposite should however be interpreted with caution. As discussed briefly in Section 3.1, reaching a steady state takes a considerable time (thousands of orbits). Before the steady state is reached, the planet may be able to open only a gap, which will slowly turn into a hole. We remark that 1000 orbits at 30 au is approximately 1.6×10^5 yr, which is a sizeable fraction of the disc lifetime (2–3 Myr; Fedele et al. 2010). Therefore, observing a gap does *not* necessarily mean that the planet is less massive than the previously stated threshold.

To get better estimates on the planet mass, it is thus necessary to use *quantitative* arguments. In particular, the diagnostics that have been proposed in the literature (de Juan Ovelar et al. 2013; Kanagawa et al. 2015; Akiyama et al. 2016) are the gap depth, the gap width and the location of the bright ring in the submm image.

To quantify the shape and position of the gap, we compute these quantities from our simulated images in the following way. First, we de-projected the image with the known inclination and position angles and calculated the azimuthally averaged radial surface brightness profile of the disc. We note that in reality the inclination of the disc can be constrained fairly well from submm line observations. Then we fitted a first-order polynomial in log–log space to the radial intervals [0.075 arcsec, 0.1 arcsec] and [0.45 arcsec, 0.55 arcsec] to get a model of the background surface brightness profile. We then normalized the azimuthally averaged radial surface brightness profile of the disc to the fitted polynomial. Finally, we measured the parameters of the gap on this normalized radial surface brightness profile, I_ν, between 0.1 and 0.45 arcsec.

The depth of the gap was taken to be the minimum of the normalized surface brightness, $I_{\nu,\rm min}$. The width of the gap was taken to be the distance between the two radii (inner and outer radius of the gap), where the normalized radial surface brightness dropped below $(1-0.66 \times (1-I_{\nu,\rm min}))$. The location of the bright ring in the submm was determined as the position of the maximum in the normalized surface brightness outside of the gap. It is important to note that we assumed that gaps are detectable if the surface brightness reduction in the gap is more than or equal to 50 per cent compared to the fitted background surface brightness of the disc.

Regarding the gap depth as derived from the submm images, we remark that there is only a narrow range of planet masses that is able to create gaps. The other planets either do not affect the dust surface density or create actual holes, for which measuring the contrast is not meaningful. For this reason, we caution against the use of the relations for the gap depth that have been derived for the gas (Kanagawa et al. 2015), as they are unlikely to hold when applied to submm observations and they lead to serious overestimates of the planet mass. Moreover, the gap depth is affected by the finite resolution of the observations, which makes the gap shallower than what it would be in an image with infinite resolution.

The gap width as measured from the submm images suffers from the same problem, namely that for the most massive planets the gaps will slowly turn into holes for which a width is no longer defined. We thus consider in what follows the gap width as measured from the SPHERE NIR images. The results are plotted in Fig. 16. Note that in order to make the correlation between the planet mass and the gap width independent of both the distance to the system and of the distance between the planet and the star, we normalized the gap width with the distance of the gap centre from the star. Finally, to stress more the dependence on the planet mass, we show in the figure the cube of the gap width. From the theoretical point of view, this is justified by the fact that we expect the gap width to be set by the Hill radius of the planet, and we thus expect the quantity we plot to scale linearly with the planet mass. We can see how the gap width is a good estimator of the planet mass. As discussed in Section 3.1, there is still some time evolution on the time-scale of $\sim 10^3$ orbits, and therefore we show the correlation at two different times (400 and 3000 orbits) to bracket the importance of time evolution. A linear fit to the data points in the form of $\log y = C_0 + C_1 \log x$ (where the logarithms are in base 10) results in coefficients of $C_0 = -2.981$, $C_1 = 0.797$ and $C_0 = -3.953$, $C_1 = 1.143$ for 400 and 3000 planetary orbits, respectively. The masses derived from the relations presented here should then be considered only as lower limits in case the gap is created by a more massive planet at earlier times. The uncertainty in the planet mass determination is a factor of 2–3, although we stress that, unless the planet is very young,

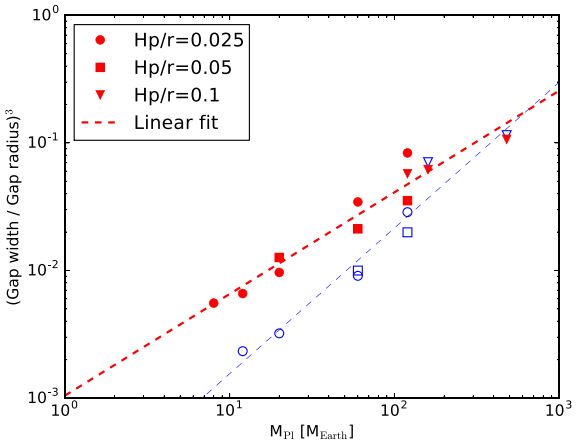

Figure 16. Gap width derived from the scattered light observations (normalized to the gap distance from the star, and to the third power to stress more the dependence on the planet mass), as a function of the planet mass at the time of 400 (blue symbols) and 3000 (red symbols) planetary orbits. The different markers indicate the different aspect ratios and we show a linear fit. While a clear and tight correlation holds between the gap width and the planet mass at any given time, the correlation evolves in time, which leads to a factor of a few uncertainty in planet mass if the system is very young. Note that gap width does not depend on the disc temperature, but the gap depth does. The reason why the points for different aspect ratios cover different ranges in planet masses is that in a warmer disc a higher planet mass is required to open a gap. The planet masses assume a star of 1 $M_\odot$. For stars of different masses, the mass should be rescaled to the same mass ratio accordingly.

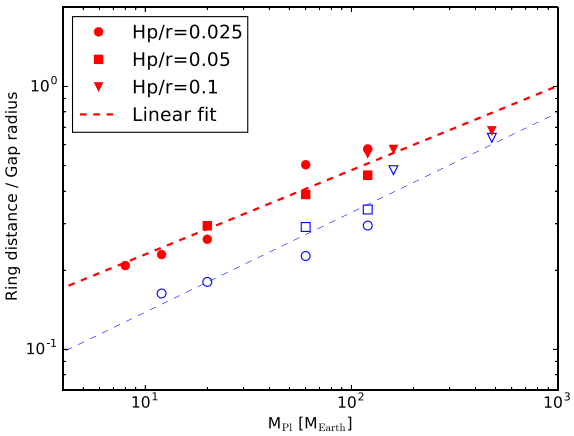

Figure 17. Ratio of the radial distance of the pressure maximum outside the planet orbit (as derived from the submm image) from the location of the planet (reconstructed using the centre of the gap in the NIR image) to the radius of the gap centre as a function of planet mass. The correlation is evident and it holds even when varying the disc aspect ratio (indicated by the marker). However, it varies with time as the two sets of points show (blue data points: 400 orbits; red data points: 3000 orbits), so that the planet mass derived from the final correlation can be considered only as a lower limit on the planet mass, as one cannot exclude that the system is very young. The planet masses assume a star of 1 $M_\odot$. For stars of different masses, the mass should be rescaled to the same mass ratio accordingly.

observations are more likely to target planets where the gap width has reached convergence. Note also that there is no need to have any knowledge of the disc temperature to do this plot; quantities that can be derived directly from the observations are sufficient. This is because, as already mentioned, the gap width is mostly set by the Hill radius of the planet (see Duffell & MacFadyen 2013 for a discussion about the regimes where this holds).

One needs to keep in mind though that while the gap width does not depend on the disc temperature, the gap depth does, and the same planet in a colder disc creates a deeper gap. Along the same line, in a warmer disc a more massive planet is necessary to create a gap that is deep enough to be observed (which is the reason why the points for different aspect ratios cover different ranges in planet masses).

Finally, the third diagnostic that we consider is the radial distance of the maximum in the submm images from the planet location. This is similar to what has been proposed in the context of transition discs (de Juan Ovelar et al. 2013), namely that the different location of the holes at different wavelengths (normally scattered light in comparison with submm) is the smoking gun for the presence of a pressure maximum, and in theory this effect can be used to measure the planet mass. For the planet masses that we consider, we have shown how the scattered light images always show gaps rather than holes. We can therefore use the image to pinpoint the radial location of the planet, which we assume to be at the centre of the gap. In transition discs instead one has to resort to use the inner edge of the NIR image (as there might be a hole). We can then use the submm image to find the maximum in the dust surface density, which traces the pressure maximum in the gas. This method thus requires two observations at different wavelengths. While we use NIR and submm in what follows, the requirement for the first wavelength is to show a gap rather than a hole (so that one can constrain the radial position of the planet) and for the second one to exhibit a maximum in the surface brightness at the pressure maximum location. In Fig. 17, we show the ratio of the radial distance of the maximum from the location of the planet as a function of the planet mass estimated from the simulated observations at 400 orbits and at 3000 orbits of the planet. To make the plot independent of both the distance to the system and the distance of the planet from the star, we normalize the radial distance of the maximum from the planet by the distance of the gap centre from the star. As can be seen, the correlation between the position of the maximum and the planet mass is clear and tight at each epoch, even though a clear time evolution is also present in the figure as in the previous case, since the position of the maximum moves further away from the gap with time (see Section 3.1). As shown in Fig. 3, the position of the maximum has reached convergence after 3000 orbits, so that the red points are representative of the subsequent evolution. A linear fit to the data points in the form of $\log y = C_0 + C_1 \log x$ (where, like before, the logarithms are in base 10) results in coefficients of $C_0 = -1.238$, $C_1 = 0.379$ and $C_0 = -0.959$, $C_1 = 0.320$ for the points at 400 and 3000 planetary orbits, respectively.

Given that we expect the quantities plotted to scale with the intensity of the pressure forces, the existence of a correlation shows that the distance of the pressure maximum must scale with the Hill radius (as is the case for the gap width). Indeed, this is confirmed by performing a fit to the distance normalized by the disc scaleheight as a function of the planet mass normalized to the gap opening mass, which shows how the distance of the submm ring Δ_{mm} is $\Delta_{mm} \simeq 10(M_{pl}/M_{th})^{1/3} H = 10R_H$ after 3000 orbits (the same result can be obtained from the coefficients of the fit given above). Using non-normalized quantities has the advantage, though, that it is not required to know the disc temperature. The same caveats as before about the fact that it is the disc temperature that sets the minimum threshold mass still hold. We also experimented with, instead of using the simulated observations, deriving the same quantity from the gas surface density, where we can also measure the locations of the planet and of the pressure maximum. No noticeable difference

is found for the pressure maximum position, which shows that this quantity is a very robust indicator of the planet mass as from *dust* (continuum) observations one can reconstruct fundamental properties of the (unseen) *gas* disc. Our method instead systematically slightly underestimates the position of the planet, which we attribute to radiative transfer effects. The error doubles in the final estimate as we normalize the distance to the gap centre. Using directly the values from the simulations yields then a slightly different coefficient $C_0 \simeq -1.1$, or $\Delta_{\rm mm} \simeq 7.5 R_{\rm H}$.

Of the two criteria that we discussed, the gap width has the advantage of requiring observations only at one wavelength. However, it needs to be borne in mind that scattered light observations have a slightly higher threshold mass for observability. Moreover, experimenting with deriving a gap width has shown us how the gap width is somehow sensitive to the exact way the fit is done and to the details of the gap shape. The position of the pressure maximum has instead the advantage of being straightforward to apply and requiring little manipulation of the data.

5.2 Prospects for the future

While currently there are no instruments in operation in the MIR with sufficiently high resolution for detecting low-mass planets, the 30 m telescope class will be a great improvement. It will provide the same resolution we have currently with SPHERE or ALMA. This work shows that the thermal emission of the disc in the MIR is a good wavelength to use to probe the structures sculpted by planets in the disc.

However, the hard boundary in the planet mass that we discuss in this paper is set by an intrinsic property, that is, how strong is the perturbation in the dust, rather than by a limitation in angular resolution. The only requirement on the angular resolution is that it is sufficient to detect the presence of a gap (if it is there). While the resolutions we considered in this paper are enough for reaching the 'intrinsic' boundary (i.e. resolving the gap width for a planet of the minimum mass required to open a gap in the dust) at 30 au, improvements in spatial resolution in the future will still allow us to observe planets closer to the star or in discs further from Earth.

5.3 Limitations and other effects

We assumed that the planet is at several tens of au. Although very little is known about planets at these locations (with only a handful of planets around main-sequence stars detected by direct imaging; Chauvin et al. 2015), this choice is backed up by an image like HL Tau. Although other interpretations for the gap structure (which do not invoke the presence of planets) have been proposed so far (Zhang, Blake & Bergin 2015), if planets are responsible for the observed morphology, it means that they can form at these large orbital distances and be found in protoplanetary discs. Recent observations of LkCa15 (Sallum et al. 2015) also point in the same direction; moreover, a common explanation of transition discs (see Espaillat et al. 2014 for a review) is the presence of massive planets at tens of au. The presence of a super-Earth at tens of au is particularly challenging to explain by theoretical models as in core accretion the time-scale for forming planets at these orbital distances is longer than the disc lifetime (but see Lambrechts & Johansen 2012 for an alternative), while gravitational instability tends to form much more massive objects. A possibility (Ida, Lin & Nagasawa 2013; Kikuchi, Higuchi & Ida 2014) is that they have been scattered by giant planets that formed closer to the star. If they manage to accrete gas, they might eventually turn into very massive giants ($\gtrsim 10 M_J$) given that most of the mass is in the outer part of the disc.

In this work, we assumed a constant Stokes number – we did not include dust coagulation and fragmentation. Due to numerical limitations, no work so far has implemented a full dust evolution model on top of a hydro simulation, although approximate attempts have been done (Gonzalez et al. 2015), or just static snapshots from the hydro simulation have been used (Pinilla et al. 2012a; de Juan Ovelar et al. 2013). This is an aspect that is worth exploring in future works given that the time-scales that we have run our simulations for are a sizeable fraction of the disc lifetime. In addition, it has been proved that dust evolution alone can create gaps in scattered light images (Birnstiel et al. 2015), and therefore is important to disentangle the two effects. Our implementation also contains no feedback of the dust on to the gas. However, this is a minor limitation for the lowest mass planets we simulate (which are the real focus of this paper) given the modest amount of dust pile-up at the outer edge of the gap.

Our simulations are not 3D, a limitation that we share with other works that have been done in this area (Zhu et al. 2012; Dong et al. 2015; Picogna & Kley 2015). This is unlikely to affect the big grains, whose dynamics is limited to the mid-plane due to settling. In addition, at long wavelengths discs are optically thin so that observations probe the disc mid-plane. If there is a vertical dependence of the dynamics, it might however affect the small dust since observations at short wavelengths (i.e. in scattered light) probe only the surface of the disc. In particular, the temperature and the stopping time depend on the height above the mid-plane – in addition there might be vertical motions (e.g. Morbidelli et al. 2014; Fung, Artymowicz & Wu 2015) that complicate the picture even more. This should be explored in future papers. We remark in particular that, of the two ways of estimating the planet mass that we discussed, this affects mostly the NIR gap width, which therefore we regard as more uncertain. Given that the other method we propose instead uses the NIR image only to pinpoint at the radial location of the planet, we expect it to be resilient to potential 3D effects.

We did not include migration. Taken at face value, the relevant migration rate, type I, is very fast (Tanaka, Takeuchi & Ward 2002), so that our approximation might not appear fully justified. However, it is known that such a rate is not compatible with the observed properties of exoplanetary systems (Ida & Lin 2008), and a reduction in the migration rate of almost two orders of magnitude is needed to reconcile with exoplanet statistics. While there is considerable debate on the physical reasons (e.g. Masset et al. 2006; Bitsch & Kley 2011; Hasegawa & Pudritz 2011), all explanations require additional physics which is not present in our simulation. Therefore, in light of these results, it is safe to say that the migration rate as computed in our locally isothermal simulation would not be the correct one anyway. We plan to explore this effect too in future papers. Finally, it should be added that recent research (e.g. Lyra, Paardekooper & Mac Low 2010; Bitsch et al. 2014) has also highlighted the existence of zero-torque radii where the type I migration rate vanishes. The effectiveness of these 'safe' locations depends on the planet mass (Bitsch et al. 2013), favouring planet masses around $\sim 20\,{\rm M}_\oplus$. If the planet is at one of those locations, which might be likely as migration converges towards them, then neglecting migration as we have done in this paper is justified.

Finally, we were limited to study dust smaller than ${\rm St} = 1$ by the choice of modelling dust as a fluid. In practice, given that the planets that we simulate in this paper only open shallow gaps, this is not a real limitation. Using particles rather than a fluid we could study bigger dust, but dust diffusion, which we showed to be an important

contribution in setting the dust radial velocity, would have been considerably more difficult to implement.

6 CONCLUSIONS

In this paper, we have undertaken a systematic study to establish how the observational signatures of low-mass planets embedded in protoplanetary discs depend on the disc properties. We can conclude that the following.

(i) Low-mass planets (tens of $M_\oplus$), even if they are not fully in the gap opening regime, can generate observational signatures in protoplanetary discs, consisting in a gap at the radial location of the planet and a bright ring at the gap edge.

(ii) The observational signatures are always azimuthally symmetric.

(iii) In terms of current facilities, we find that the observational signatures can be traced both in the submm (with ALMA) and in the scattered light (with instruments such as SPHERE or GPI). We have highlighted how the observational signatures are present also in the MIR, which will become observable with the upcoming generation of 30 m class telescopes.

(iv) For an aspect ratio H/R of 0.05, the threshold to perturb the dust surface density is $\sim 15\,M_\oplus$, with some dependence on the wavelength of the observations which favours the submm. In particular, the threshold is closer to $\sim 12\,M_\oplus$ in the submm and $\sim 20\,M_\oplus$ in the NIR or MIR. More importantly, though, the threshold is highly dependent (roughly with the third power) on the disc aspect ratio. We predict thus that the minimum mass is $\sim 15((H/R)/0.05)^3\,M_\oplus$. This is an *intrinsic* boundary.

(v) Real observations are limited though by the finite resolution. We show that at the fiducial distance of 30 au from the star, the threshold for detection with existing instruments in the NIR and submm and planned instruments in the MIR is set by the intrinsic properties of the disc. Improvements in the telescope capabilities will allow us to sample regions closer to the star.

(vi) We find (in agreement with Lambrechts et al. 2014) that a planet mass $\gtrsim 0.2 M_{\rm th} \sim 20((H/R)/0.05)^3\,M_\oplus$ is required to create a pressure maximum in the gas at the gap outer edge. After enough time has passed, the inescapable consequence for these planets is to create a hole in the submm dust. Planets smaller than this threshold can still affect the dust significantly and create a gap in the submm, although the relevant range of planet masses is rather limited (a planet 2.5 times less massive than the quoted threshold does not produce any observational signature).

(vii) It is interesting also to explore the inverse problem, that is, to derive the planet mass from high-resolution observations. Using the gap width or contrast in the submm (ALMA) images to measure the planet mass is complicated by the fact that the gaps will eventually turn into holes over a wide range of planet masses. We thus disfavour this method to measure the planet mass and prefer to use other diagnostics.

(viii) We find that the gap width as derived from the scattered light images is a good indicator of the planet mass. This indicator is affected by time evolution and it takes roughly 1000 orbits (which at 30 au corresponds to $\sim 1.6 \times 10^5$ yr) to reach the final value. If the system is very young, this might lead to a factor of 2–3 underestimate in the planet mass determination. Additionally, the exact definition of gap width is sensitive to the details of the gap shape.

(ix) We find also the location of the bright ring in the submm images, which traces the gas pressure maximum, to be a robust indicator of the planet mass. In the case the submm image shows a hole, it is necessary to use the scattered light image to pinpoint the radial location of the planet. We expect this method to be the most resilient to the details of the dust dynamics; the same caveats about time dependence as before apply.

ACKNOWLEDGEMENTS

We thank an anonymous referee for a careful reading of our manuscript and many useful comments. We also thank Leonardo Testi for a stimulating discussion that started this work, Sijme-Jan Paardekooper and Richard Alexander for their constructive criticism, Judith Ngoumou and the Munich Star Formation Coffee for a very lively discussion. This work has been supported by the DISCSIM project, grant agreement 341137 funded by the European Research Council under ERC-2013-ADG. This work used the DIRAC Shared Memory Processing system at the University of Cambridge, operated by the COSMOS Project at the Department of Applied Mathematics and Theoretical Physics on behalf of the STFC DiRAC HPC Facility (www.dirac.ac.uk). This equipment was funded by BIS National E-infrastructure capital grant ST/J005673/1, STFC capital grant ST/H008586/1 and STFC DiRAC Operations grant ST/K00333X/1. DiRAC is part of the National E-Infrastructure.

REFERENCES

Akiyama E., Hasegawa Y., Hayashi M., Iguchi S., 2016, ApJ, 818, 158
Baruteau C. et al., 2014, in Beuther H., Klessen R. S., Dullemond C. P., Henning T., eds, Protostars and Planets VI. Univ. Arizona Press, Tucson, p. 667
Benisty M. et al., 2015, A&A, 578, L6
Benítez-Llambay P., Masset F., Koenigsberger G., Szulágyi J., 2015, Nature, 520, 63
Beuzit J.-L. et al., 2008, Proc. SPIE, 7014, 701418
Birnstiel T., Andrews S. M., Pinilla P., Kama M., 2015, ApJ, 813, L14
Bitsch B., Kley W., 2011, A&A, 536, A77
Bitsch B., Crida A., Morbidelli A., Kley W., Dobbs-Dixon I., 2013, A&A, 549, A124
Bitsch B., Morbidelli A., Lega E., Kretke K., Crida A., 2014, A&A, 570, A75
Brogan C. L. et al., ALMA Partnership, 2015, ApJ, 808, L3
Chauvin G. et al., 2015, A&A, 573, A127
Clarke C. J., Pringle J. E., 1988, MNRAS, 235, 365
Crida A., Morbidelli A., Masset F., 2006, Icarus, 181, 587
de Juan Ovelar M., Min M., Dominik C., Thalmann C., Pinilla P., Benisty M., Birnstiel T., 2013, A&A, 560, A111
de Val-Borro M. et al., 2006, MNRAS, 370, 529
Dipierro G., Price D., Laibe G., Hirsh K., Cerioli A., Lodato G., 2015, MNRAS, 453, L73
Dipierro G., Laibe G., Price D. J., Lodato G., 2016, MNRAS, 459, L1
Dong R., Zhu Z., Whitney B., 2015, ApJ, 809, 93
Duffell P. C., MacFadyen A. I., 2013, ApJ, 769, 41
Espaillat C. et al., 2014, in Beuther H., Klessen R. S., Dullemond C. P., Henning T., eds, Protostars and Planets VI. Univ. Arizona Press, Tucson, p. 497
Fedele D., van den Ancker M. E., Henning T., Jayawardhana R., Oliveira J. M., 2010, A&A, 510, A72
Fouchet L., Gonzalez J.-F., Maddison S. T., 2010, A&A, 518, A16
Fung J., Shi J.-M., Chiang E., 2014, ApJ, 782, 88
Fung J., Artymowicz P., Wu Y., 2015, ApJ, 811, 101
Garaud P., Barrière-Fouchet L., Lin D. N. C., 2004, ApJ, 603, 292
Garufi A. et al., 2013, A&A, 560, A105
Gonzalez J.-F., Pinte C., Maddison S. T., Ménard F., Fouchet L., 2012, A&A, 547, A58
Gonzalez J.-F., Laibe G., Maddison S. T., Pinte C., Ménard F., 2015, MNRAS, 454, L36

Hasegawa Y., Pudritz R. E., 2011, MNRAS, 417, 1236
Howard A. W. et al., 2012, ApJS, 201, 15
Ida S., Lin D. N. C., 2008, ApJ, 673, 487
Ida S., Lin D. N. C., Nagasawa M., 2013, ApJ, 775, 42
Jin S., Li S., Isella A., Li H., Ji J., 2016, ApJ, 818, 76
Juhász A., Benisty M., Pohl A., Dullemond C. P., Dominik C., Paardekooper S.-J., 2015, MNRAS, 451, 1147
Kanagawa K. D., Muto T., Tanaka H., Tanigawa T., Takeuchi T., Tsukagoshi T., Momose M., 2015, ApJ, 806, L15
Kenyon S. J., Hartmann L., 1995, ApJS, 101, 117
Kikuchi A., Higuchi A., Ida S., 2014, ApJ, 797, 1
Lambrechts M., Johansen A., 2012, A&A, 544, A32
Lambrechts M., Johansen A., Morbidelli A., 2014, A&A, 572, A35
Ligi R. et al., 2012, A&A, 545, A5
Ligi R. et al., 2016, A&A, 586, A94
Lin D. N. C., Papaloizou J., 1979, MNRAS, 186, 799
Lin D. N. C., Papaloizou J. C. B., 1993, in Levy E. H., Lunine J. I., eds, Protostars and Planets III. Univ. Arizona Press, Tucson, p. 749
Lyra W., Paardekooper S.-J., Mac Low M.-M., 2010, ApJ, 715, L68
Masset F., 2000, A&AS, 141, 165
Masset F. S., Morbidelli A., Crida A., Ferreira J., 2006, ApJ, 642, 478
Mayor M., Queloz D., 1995, Nature, 378, 355
Morbidelli A., Szulágyi J., Crida A., Lega E., Bitsch B., Tanigawa T., Kanagawa K., 2014, Icarus, 232, 266
Morbidelli A., Lambrechts M., Jacobson S., Bitsch B., 2015, Icarus, 258, 418
Muto T. et al., 2012, ApJ, 748, L22
Owen J. E., 2014, ApJ, 789, 59
Owen J. E., Wu Y., 2013, ApJ, 775, 105
Paardekooper S.-J., Mellema G., 2004, A&A, 425, L9
Paardekooper S.-J., Mellema G., 2006, A&A, 453, 1129
Picogna G., Kley W., 2015, A&A, 584, A110
Pinilla P., Birnstiel T., Ricci L., Dullemond C. P., Uribe A. L., Testi L., Natta A., 2012a, A&A, 538, A114
Pinilla P., Benisty M., Birnstiel T., 2012b, A&A, 545, A81
Pollack J. B., Hubickyj O., Bodenheimer P., Lissauer J. J., Podolak M., Greenzweig Y., 1996, Icarus, 124, 62
Raymond S. N., Kokubo E., Morbidelli A., Morishima R., Walsh K. J., 2014, in Beuther H., Klessen R. S., Dullemond C. P., Henning T., eds, Protostars and Planets VI. Univ. Arizona Press, Tucson, p. 595
Regály Z., Juhász A., Sándor Z., Dullemond C. P., 2012, MNRAS, 419, 1701
Rice W. K. M., Armitage P. J., Wood K., Lodato G., 2006, MNRAS, 373, 1619
Ruge J. P., Wolf S., Uribe A. L., Klahr H. H., 2013, A&A, 549, A97
Ruge J. P., Wolf S., Uribe A. L., Klahr H. H., 2014, A&A, 572, L2
Sallum S. et al., 2015, Nature, 527, 342
Shakura N. I., Sunyaev R. A., 1973, A&A, 24, 337
Stone J. M., Norman M. L., 1992, ApJS, 80, 753
Takeuchi T., Lin D. N. C., 2002, ApJ, 581, 1344
Tanaka H., Takeuchi T., Ward W. R., 2002, ApJ, 565, 1257
Varnière P., Quillen A. C., Frank A., 2004, ApJ, 612, 1152
Varnière P., Bjorkman J. E., Frank A., Quillen A. C., Carciofi A. C., Whitney B. A., Wood K., 2006, ApJ, 637, L125
Wagner K., Apai D., Kasper M., Robberto M., 2015, ApJ, 813, L2
Weidenschilling S. J., 1977, MNRAS, 180, 57
Weingartner J. C., Draine B. T., 2001, ApJ, 548, 296
Williams J. P., Cieza L. A., 2011, ARA&A, 49, 67
Zhang K., Blake G. A., Bergin E. A., 2015, ApJ, 806, L7
Zhang K., Bergin E. A., Blake G. A., Cleeves L. I., Hogerheijde M., Salinas V., Schwarz K. R., 2016, ApJ, 818, L16
Zhu Z., Nelson R. P., Dong R., Espaillat C., Hartmann L., 2012, ApJ, 755, 6
Zhu Z., Stone J. M., Rafikov R. R., Bai X.-n., 2014, ApJ, 785, 122

This paper has been typeset from a TEX/LATEX file prepared by the author.